A new kind of superimposing morphology for enhancing the light scattering in thin film silicon solar cells: Combining random and periodic structure*

Huang Zhen-Hua(黄振华)[a)b)c)], Zhang Jian-Jun(张建军)[a)b)c)†], Ni Jian(倪 垚)[a)b)c)], Wang Hao(王 昊)[a)b)c)], and Zhao Yin(赵 颖)[a)b)c)]

[a)] *Institute of Photo-electronics Thin Film Devices and Technique of Nankai University, Tianjin* 300071, *China*
[b)] *Key Laboratory of Photo-electronics Thin Film Devices and Technique of Tianjin, Tianjin* 300071, *China*
[c)] *Key Laboratory of Photo-electronic Information Science and Technology of Ministry of Education (Nankai University), Tianjin* 300071, *China*

(Received 21 September 2013; revised manuscript received 1 February 2014; published online 10 June 2014)

In this article, a new type of superimposing morphology comprised of a periodic nanostructure and a random structure is proposed for the first time to enhance the light scattering in silicon-based thin film solar cells. According to the framework of the Reyleigh–Sommerfeld diffraction algorithm and the experimental results of random morphologies, we analyze the light-scattering properties of four superimposing morphologies and compare them with the individual morphologies in detail. The results indicate that the superimposing morphology can offer a better light trapping capacity, owing to the coexistence of the random scattering mechanism and the periodic scattering mechanism. Its scattering property will be dominated by the individual nanostructures whose geometrical features play the leading role.

Keywords: light scattering, superimposing morphology, random, periodic

PACS: 42.79.–e, 88.50.gj, 88.40.jj **DOI:** 10.1088/1674-1056/23/8/084205

1. Introduction

Light trapping in thin film silicon solar cells has become an attractive research topic in recent years, for it can increase the effective optical path in the thin absorber layers and is an essential scheme to enhance the conversion efficiency of the solar cells. It is usually achieved by modulating the textured interfaces within the solar cells, especially the interfaces between the transparent-conductive-oxide (TCO) layers and the silicon-based absorber layers, and the interfaces between the back reflectors and the absorber layers.

For a typical p–i–n configuration in which the solar cells are deposited on the TCOs in the order of B-doped window layers, intrinsic layers, and P-doped layers, the interface between the TCO layer and the B-doped window layer plays an essential role.[1] So the surface morphologies of TCOs are widely studied both experimentally and theoretically in order to obtain TCO/silicon interfaces with the best scattering properties. Generally, the morphologies are developed in two different directions: random structure and periodic structure.

The typical random structure, which includes Asashi-U or Asahi-W type SnO_2:F,[2] pyramidal-like ZnO:B,[3] and crater-like ZnO:Al,[4] can scatter the light into a continuous range of angles and it is predicted to approach to the classical optical path enhancement limit $4n^2$, where n is the refractive index of the absorber.[5] The periodic structures, which include nanocavities,[6] self-ordered dimple patterns[7] or nanodomes,[8] can only scatter the light into discrete angles but has the potential to break the $4n^2$ limit as predicted by Yu and Fan's theory.[9] In most of the literature, these two types of nanostructures are studied separately and are occasionally compared with each other to show which capability of light trapping is better.[10] However, the combination of the random structure and the periodic structure is barely considered and reported. As shown in Fig. 1, when a layer with a periodic morphology (see Fig. 1(a)) is stacked on a layer with a random morphology (see Fig. 1(b)), the resulting morphology of the stack (see Fig. 1(c)) will succeed in both the random and periodic features. According to Isabella *et al.*'s work,[11] this new superimposing morphology is possible to achieve a higher scattering level in a broad wavelength range due to the coexistence of the random and periodic scattering mechanisms. Besides, it is also realizable to transform this kind of complicated morphology to the TCO surfaces from opaque moulds via the nano-imprint lithography technique recently developed by Battaglia *et al.*[12,12,14] In order to explore the potential of light-trapping in this new superimposing morphology, a theoretical study of its scatting properties is first needed.

*Project supported by the National Basic Research Program of China (Grant Nos. 2011CBA00705, 2011CBA00706, and 2011CBA00707), the National Natural Science Foundation of China (Grant No. 61377031), the Natural Science Foundation of Tianjin, China (Grant No. 12JCQNJC01000), the Specialized Research Fund for the Doctoral Program of Higher Education, China (Grant No. 20120031120044), and the Fundamental Research Funds for the Central Universities, China (Grant No. 65012371).

†Corresponding author. E-mail: jjzhang@nankai.edu.cn

© 2014 Chinese Physical Society and IOP Publishing Ltd

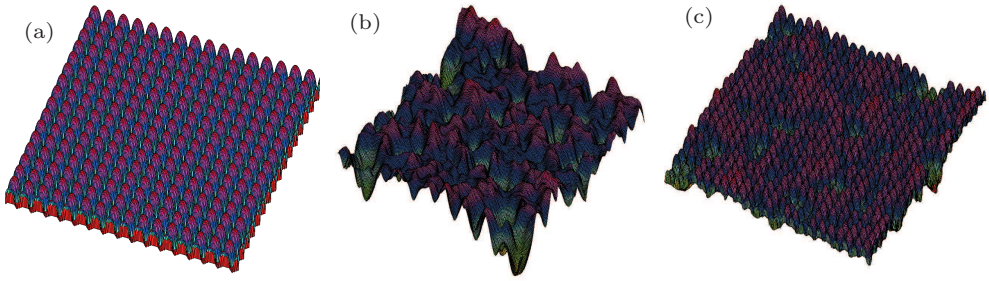


Fig. 1. (color online) (a) Hemisphere-like periodic morphology, (b) random morphology, and (c) superimposing morphology composed of morphologies (a) and (b).

In this article, four types of superimposing morphologies based on four types of random morphologies will be considered and their scattering properties will be analyzed under the theoretical framework of the Reyleigh–Sommerfeld diffraction algorithm.[10,15,16] The similarities and dissimilarities in the light-scattering property between the superimposing morphologies and the individual morphologies will be discussed in detail.

2. Theory

The Reyleigh–Sommerfeld diffraction algorithm recently proposed by the IMT group[10,15] is a method to model the light scattering properties from the surface profile. The physical morphology of a texture surface measured with atomic force microscopy (AFM) is usually characterized by its height $Z(x,\ y)$ which is a function of the lateral coordinates x, y. As shown in Fig. 2, when light passes across the textured interface from the first medium with refractive index n_1 to the second medium with refractive index n_2, scattering will take place. The scattering properties of the interface are usually described by two parameters:[17] the haze parameter, $H(\lambda)$, which is the ratio between the scatted part of the transmitted (reflected) light and the total transmitted (reflected) light, and the angular distribution function (ADF) of the transmitted (reflected) light. The Reyleigh–Sommerfeld method then establishes a relationship between $Z(x,y)$ and $H(\lambda)$, ADF via a physical quantity, and the radiance L.[16] In the case of transmission discussed in this article, the radiance L in direction cosine space for a given wavelength λ is given by Eq. (1)

$$L(\alpha,\beta,\lambda) = C(\lambda)\cdot\left|\iint \mathrm{d}x\cdot\mathrm{d}y\cdot\exp\left[2\pi\mathrm{i}\cdot\frac{n_2}{\lambda}\cdot(\alpha x+\beta y)\right]\right. \times \left.\exp\left[2\pi\mathrm{i}\cdot\frac{|n_1-n_2|}{\lambda}\cdot Z(x,y)\right]\right|^2. \quad (1)$$

Here, $C(\lambda)$ is a wavelength-dependent normalization constant, and α and β are the direction cosines in reciprocal space. Then by using the equations $\alpha=\sin\theta\cos\varphi$ and $\beta=\sin\theta\sin\varphi$, the radiance L can be transformed into projected spherical coordinates $(\theta,\ \varphi)$. In order to satisfy the conservation law of energy, L also needs to be normalized via Eq. (2)

$$\int_0^{\pi/2}\mathrm{d}\theta\int_0^{2\pi}\mathrm{d}\varphi\cdot\sin\theta\cdot\cos\theta\cdot L(\theta,\varphi,\lambda)=1. \quad (2)$$

Then the angular distribution function of the transmitted light $ADF(\theta,\lambda)$ which represents the total amount of intensity scattered into the narrow range $\mathrm{d}\theta$ centering around the given polar angle θ is obtained from the following expression:

$$ADF(\theta,\lambda)=\int_0^{2\pi}\mathrm{d}\varphi\cdot\sin\theta\cdot\cos\theta\cdot L(\theta,\varphi,\lambda). \quad (3)$$

The haze parameter for transmission $H_{\mathrm{T}}(\lambda)$ can be obtained from the following expression

$$H_{\mathrm{T}}(\lambda)=\int_{\theta>0}^{\pi/2}\mathrm{d}\theta\int_0^{2\pi}\mathrm{d}\varphi\cdot\sin\theta\cdot\cos\theta\cdot L(\theta,\varphi,\lambda). \quad (4)$$

Since L is influenced by n_1 and n_2 as shown in Eq. (1), it should be pointed out that the $ADF(\theta,\lambda)$, $H_{\mathrm{T}}(\lambda)$ of the TCO/air interface, which can be measured experimentally, is totally different from those of the TCO/silicon interface, which is not directly accessible but can truly describe the scattering properties of the TCO's morphologies in the solar cells.[17,18]

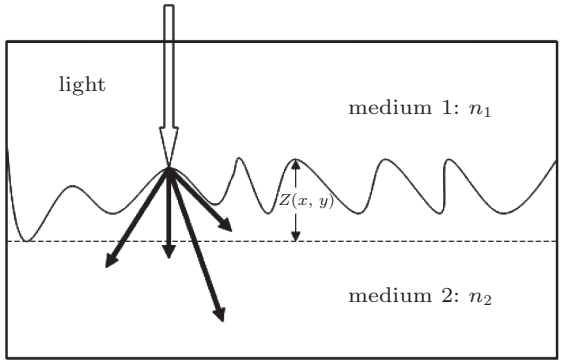


Fig. 2. Schematic digram for the Reyleigh–Sommerfeld diffraction algorithm.

3. Result and discussion

3.1. Verification of the theory

Four types of random morphologies with different root mean square (rms) roughness values and peak-to-valley (PV)

distances are taken into account and their detailed parameters are listed in Table 1. Their morphologies are obtained by AFM (nanonavi SPA-400 SPM) in a contact mode and the images are shown in Fig. 3. The scanning area is set to be 20 μm × 20 μm in order to grasp the statistical feature of the morphology as completely as possible and to enhance the accuracy of the successive calculation. Their specular transmission spectra T_{spec} and total transmission spectra T_{tot} are measured by an UV-Vis-NIR (Varian,Carry 5000) spectrophotometer with an integrating sphere in a wavelength range from 300 nm to 1200 nm and plotted in Fig. 4(a), respectively. As the optical bandgap (E_{opt}) of SnO_2:F is higher than that of ZnO:Al, it can be observed that T_{spec} and T_{tot} curves of SnO_2:F rise up earlier than those of the other three types of ZnO:Al. It can also be found that as the increases of rms and PV from type A to type D, the interference patterns shown in the transmission spectra become weaker and disappear gradually, and the value of T_{spec} becomes smaller. This result demostrates that as the morphologies turns rougher, the amount of light scattered becomes larger and the light turns non-coherent.

Table 1. Detailed parameters of the four types of random morphologies.

Type	Material	Time of wet-etching by 0.5% HCl/s	Morphology	rms/nm	PV/nm
A	asahi U type SnO_2:F	NO	pyramidal-like	38	336
B	sputtering ZnO:Al	10	crater-like	59	462
C	sputtering ZnO:Al	15	crater-like	78	520
D	sputtering ZnO:Al	35	crater-like	195	1495

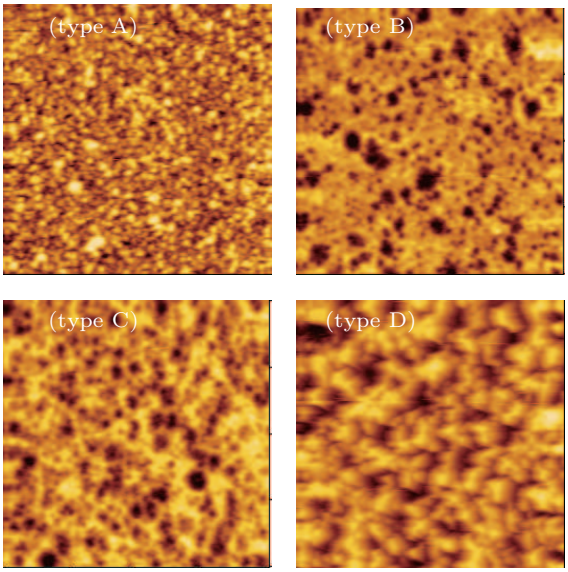


Fig. 3. (color online) AFM surface data of four types of substrates. Type A: SnO2:F rms = 38 nm, PV = 336 nm; type B: ZnO:Al rms = 59 nm, PV = 462 nm; type C: ZnO:Al rms = 77 nm, PV = 532 nm; type D: ZnO:Al rms = 195 nm, PV = 1495 nm 30 s. Image dimensions are all 20 μm×20 μm.

According to the measured T_{spec} and T_{tot}, the haze paramters of the TCO/air interfaces $H_{T-meas}(\lambda)$ are determined by $H_{T-meas}(\lambda) = (T_{tot} - T_{spec})/T_{tot}$ and plotted with solid lines in Fig. 4(b). Besides, the transmission haze values, $H_{T-cal}(\lambda)$ of the TCO/air interfaces for the four types of morphologies are calculated based on the AFM data by the Reyleigh–Sommerfeld method in Section 2 and they are plotted in symbol lines in Fig. 4(b). The wavelength-dependent refractive indices of SnO_2:F and ZnO:Al requested in Eq. (1) are adopted from Ref. [15] and the refractive index of air is set to be 1 identically. The $Z(x,y)$ values are transformed from the AFM images by the data processing software of NanoNavi SPA400. All the calculations in Eqs. (1)–(4) are done by the Matlab software, and the double integral in Eq. (1) is dealt with by the fast Fourier transform (FFT) method.

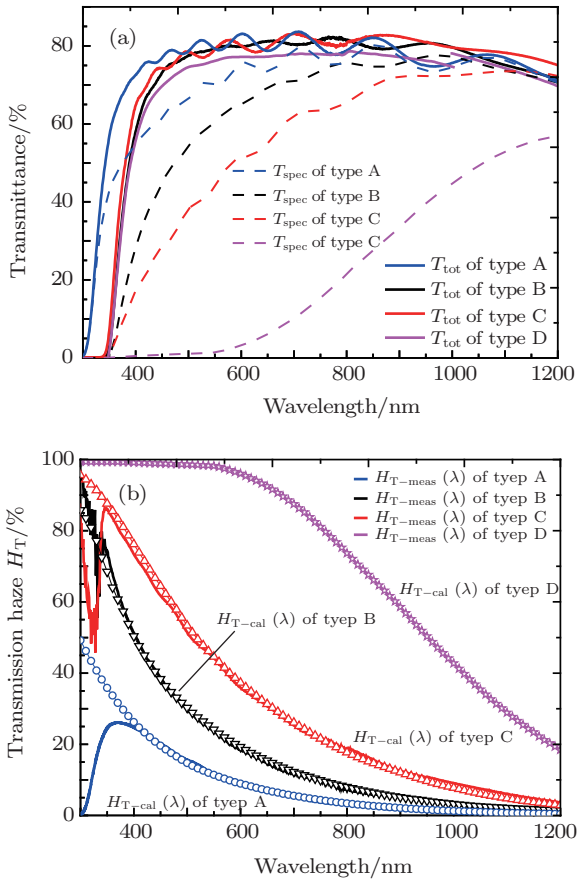


Fig. 4. (color online) (a) Specular and total transmittance T_{spec} and T_{tot} of type A, type B, type C, type D substrates; (b) measured transmission haze $H_{T-meas}(\lambda)$ and calculated transmission haze $H_{T-cal}(\lambda)$.

As shown in Fig. 4(b), the H_{T-cal} (λ) curves take on smooth and monotonically decreasing shapes in the whole region, and they match very well with the $H_{T-meas}(\lambda)$ curves in a range from 350 nm to 1200 nm. Since the thickness values of the TCO layers are assumed to be infinite in the calculation

of $H_{T-cal}(\lambda)$, the coherence addition phenomenon occurring within the actual TCO layers of limited thickness values is then ignored and the $H_{T-cal}(\lambda)$ curves show no interference patterns. Thus, in the cases of types A, B, C, a slight difference between $H_{T-cal}(\lambda)$ and $H_{T-meas}(\lambda)$ curves can be found. However, in the case of type D where the light becomes totally non-coherent within its TCO layer as the morphology becomes sufficiently rough, it can be found that its T_{spec} and T_{tot} curves become smooth and its $H_{T-cal}(\lambda)$ curve coincides perfectly with its $H_{T-meas}(\lambda)$ curve.

The reasons for the differences between $H_{T-cal}(\lambda)$ and $H_{T-meas}(\lambda)$ curves in the range of 300 nm to 350 nm are distinguishing for type A and types B, C, D. For type A, this range is close to the E_{opt} of SnO_2:F, its T_{spec} and T_{tot} curves simultaneously show sharp declines and coincide with each other gradually as the wavelength decreases, and this leads to the abnormal increase of its $H_{T-meas}(\lambda)$. For types B, C, D, this range is below the E_{opt} of ZnO:Al, their T_{spec} and T_{tot} values are nearly 0, so the $H_{T-meas}(\lambda)$ values then become meaningless, and the large falling shapes in this range then come from the measurement errors. However, in the calculation of $H_{T-cal}(\lambda)$, the absorptions of SnO_2:F and ZnO:Al below and near their optical bandgaps are not taken into account, so their $H_{T-cal}(\lambda)$ curves remain a monotonic increase as the wavelength λ decreases.

Through the comparison between $H_{T-cal}(\lambda)$ and $H_{T-meas}(\lambda)$ curves, it can be verified that the Reyleigh–Sommerfeld method can precisely recreate the scattering properties in a wide range of morphologies, so we use it to dig out the scattering properties of the new kind of superimposing morphology.

3.2. Scattering properties of superimposing morphology

In this section, we start to analyze the scattering properties of the superimposing morphology, which is comprised of the type A random nanostructure and an orthogonally arrayed hemisphere-like periodic nanostructure (see Fig. 1(a)). The radius of the hemisphere is set to be 200 nm, which is close to the hemisphere rms value of type D (195 nm), and the distance between the hemispheres is set to be 30 nm, so the period of the hemisphere-like periodic nanostructure (a) is 430 nm. The $H_T(\lambda)$ parameters of the interfaces with the structure of random nanostructure/air, hemisphere-like nanostructure/air, superimposing nanostructure/air, random nanostructure/silicon absorber, hemisphere-like nanostructure/silicon absorber, and superimposing nanostructure/silicon absorber are plotted in Fig. 5 as $H_1(\lambda)$–$H_6(\lambda)$, respectively.

In the case of light scattered from the TCO layer into air, it is clearly shown that the periodic structure (see curve $H_2(\lambda)$) can achieve higher light-scattering in a short wavelength region (below 450 nm) than the type-A random structure (see curve $H_1(\lambda)$), but the latter offers better light-scattering in the remaining wavelength region. However, the complete coincidence between $H_3(\lambda)$ and $H_1(\lambda)$ in a range from 550 nm to 1200 nm and the high approximation of $H_3(\lambda)$ to $H_2(\lambda)$ in a range from 300 nm to 450 nm suggest that the superimposing structure takes advantage of both individual structures and realizes the best light-scattering.

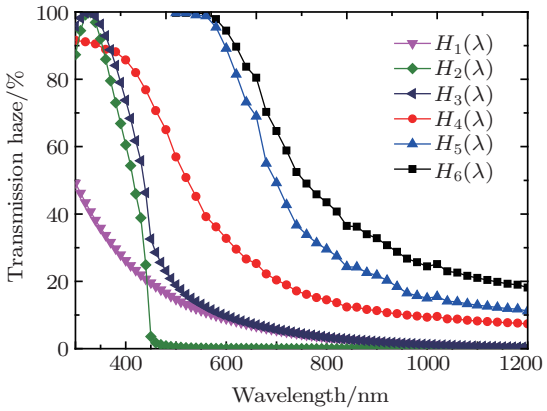


Fig. 5. (color online) Haze parameters for transmission, $H_T(\lambda)$: (a) $H_1(\lambda)$, calculated for the type-A nanostructure/air interface (down triangles); (b) $H_2(\lambda)$, calculated for the hemisphere-like nanostructure/air interface (diamonds); (c) $H_3(\lambda)$, calculated for the supermiposing nanostructure/air interface (left triangles); (d) $H_4(\lambda)$, calculated for the type-A nanostructure/silicon interface (circle); (e) $H_5(\lambda)$, calculated for the hemisphere-like nanostructure/silicon interface (up triangles); (f) $H_6(\lambda)$, calculated for the supermiposing nanostructure/silicon interface (squares).

In the case of light scattered from the TCO layer into the silicon absorber, a significant ascent from $H_1(\lambda)$, $H_2(\lambda)$, $H_3(\lambda)$ to $H_4(\lambda)$, $H_5(\lambda)$, $H_6(\lambda)$ respectively can be found first, which is because the light scattering becomes stronger as the shortened wavelength in the silicon material becomes more comparable to the geometry feature of the morphologies. It can also be found that $H_6(\lambda)$ reaches a saturation state as $H_5(\lambda)$ behaves when the wavelength is lower than 600 nm and it is much higher than $H_4(\lambda)$ and $H_5(\lambda)$ in a range from 600 nm to 1200 nm and almost equal to the sum of $H_4(\lambda)$ and $H_5(\lambda)$ in a range of 800 nm to 1200 nm. These results further prove that the superimposing morphology achieves better light-trapping than the individual structures within the solar cells.

To further analyze the fundamental scattering mechanisms behind the morphologies, we calculate the *ADF*s of these three interfaces from the TCO layer into the silicon absorber respectively, and we also introduce the integral of *ADF*, i.e.,

$$\text{Integral}(\theta,\lambda) = \int_0^{\theta} ADF(\theta,\lambda)\,\mathrm{d}\theta \tag{5}$$

to further describe the angular scattering properties intuitively and quantitatively.

First, we consider the case $\lambda = 600$ nm in which the light is almost totally scattered, and the resulting *ADF*s are shown

in Figs. 6(a1)–6(a3). The *ADF* of the type-A random nanostructure/silicon interface (ADF_1) shows an apparent continuous shape, which declines monotonically as polar angle θ increases and drops below 0.2 when θ is larger than 30°. Correspondingly, the integral of ADF_1 shows a smooth increase shape, which is almost close to 1 at $\theta = 30°$. This result demonstrates that the type A structure can scatter light only into small angles. In contrast, the *ADF* of the hemisphere-like periodic nanostructure/silicon interface (ADF_2) shows a strong discrete shape with four peaks located at $\theta = 22.7°$, $\theta = 32.8°$, $\theta = 50.4°$, and $\theta = 59.1°$, respectively. Its integral shows an apparent step profile, which rises up only at the four angles and this implies that only these four angles contribute to the scattering. Since the refractive index of silicon at $\lambda = 600$ nm equals 3.63,[19] the escaping angle from silicon to air (θ_c) is around 16°. As shown in Fig. 6(a1), the part of ADF_1 located in the range lower than θ_c is dominant and its integral reaches 94.5%, which means that most of the light scattered by the type A random surface can still probably escape from the silicon absorber. However, figure 6(a2) shows that the greater part of ADF_2 is beyond θ_c, and its value reaches 90.0%, which means that most of the scattering light can be reflected totally and internally, and it can be trapped in the silicon absorber eternally, until it becomes zero due to absorption. When light is scattered by a periodic structure into a special angle θ, the parallel component of the wave vector $k_{||}$ is demanded by the guide mode theory to be in the reciprocal space.[20] In our calculation, the periods along the x coordinate and the y coordinate are the same, so the two coordinates of its relative reciprocal space are both $2\pi/a$, then the relationship between the peaks in ADF_2 and the period a can be described as follows:

$$\frac{2\pi \cdot n}{\lambda} \cdot \sin\theta = m \cdot \frac{2\pi}{a}. \tag{6}$$

Here, m is a square root of a sum of squares of two integers. So in our case, $\theta = 22.7°$, $\theta = 32.8°$, $\theta = 50.4°$, and $\theta = 59.1°$ correspond to $m_1 = 1(\sqrt{1^2+0})$, $m_2 = 1.41(\sqrt{1^2+1^2})$, $m_3 = 2(\sqrt{2^2+0})$, and $m_4 = 2.24(\sqrt{2^2+1^2})$, respectively, and these four excited guide modes in the reciprocal space are depicted in the inset of Fig. 6(a1). Comparing the *ADF* of the superimposing nanostructure/silicon interface (ADF_3) with those of ADF_1 and ADF_2, it can be found that ADF_3 keeps the same discrete peaks as ADF_2 but their distribution is also very dense and continuous as ADF_1 behaves. This result indicates that the superimposing morphology has both random and periodic scattering characteristics, which means that it possesses two different types of scattering mechanisms at the same time. Furthermore, as shown in Fig. 7(a), the integral

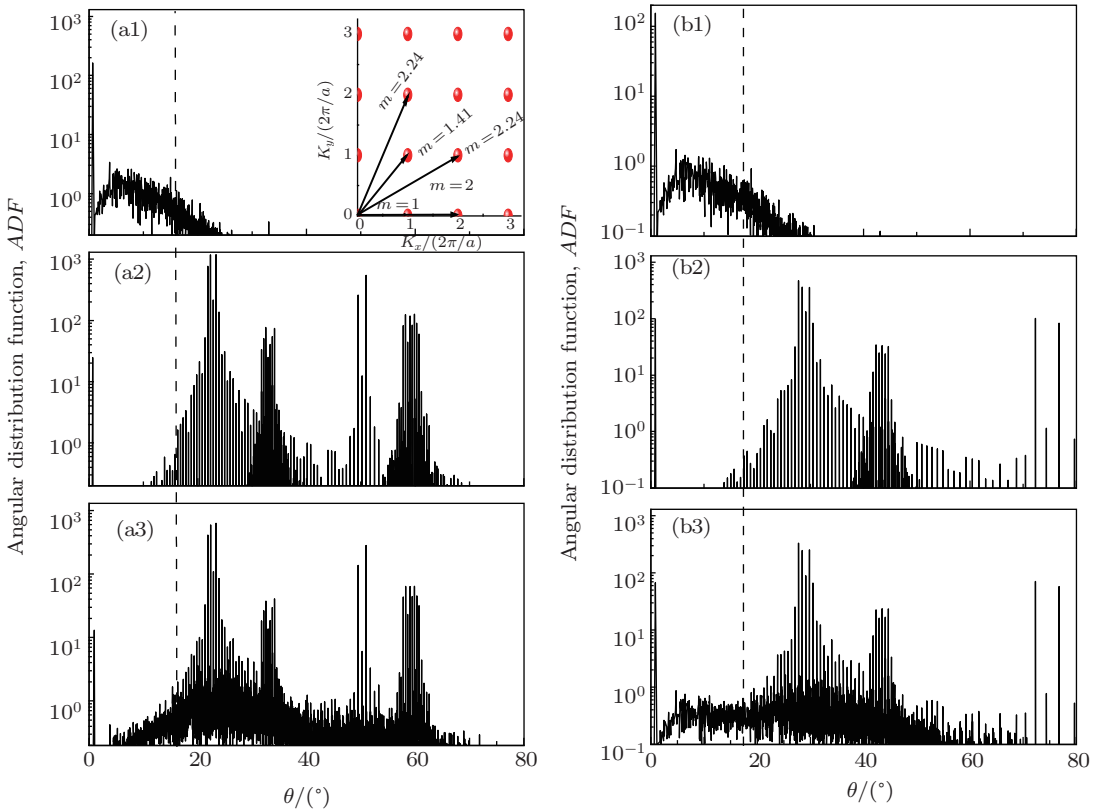


Fig. 6. (color online) Calculated angular distribution functions: (a1) ADF_1, calculated for the type-A nanostructure/silicon interface at 600 nm; (a2) ADF_2, calculated for the hemisphere-like nanostructure/silicon interface at 600 nm; (a3) ADF_3, calculated for the supermiposing nanostructure/silicon interface at 600 nm; (b1) ADF_4, calculated for the type-A nanostructure/silicon interface at 700 nm; (b2) ADF_5, calculated for the hemisphere-like nanostructure/silicon interface at 700 nm; (b3) ADF_6, calculated for the supermiposing nanostructure/silicon interface at 700 nm; inset of panel (a1) represents the reciprocal space of the hemisphere-like periodic structure.

of ADF_3 is similar to that of ADF_2, and the four discrete angles contribute to a large part of the scattering, which means that the periodic scattering mechanism plays a predominant role in this type of superimposing morphology. However, the oblique curves among these four angles in the integral of ADF_3 suggest that the random features lead to part of the light at these four angles being scattered into wide angle ranges, which can further enhance the light-trapping capacity of the superimposing morphology.

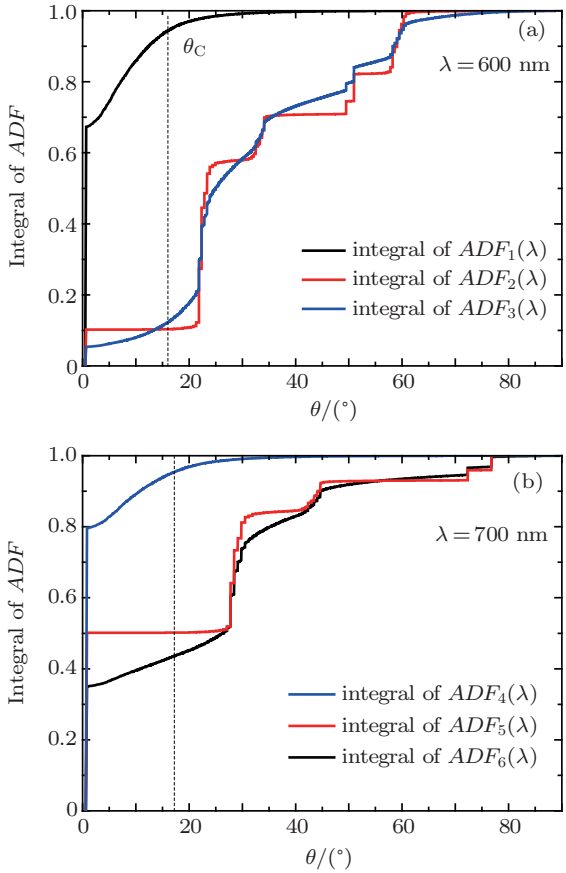


Fig. 7. (color online) Integrals of the ADFs in Fig. 6: (a) $\lambda = 600$ nm and (b) $\lambda = 700$ nm.

Secondly, the case $\lambda = 700$ nm has been calculated in which the light is partially scattered, and the resulting ADFs (ADF_4, ADF_5, ADF_6) and integrals are shown in Fig. 6(b1)–6(b3) and Fig. 7(b), respectively. Apparently, the results are similar to those in the case $\lambda = 600$ nm. ADF_6 possesses discrete peaks as ADF_5 does and continuous distributions as ADF_4 does, and its integral curves are also close to those of ADF_5, which further proves the coexistence of the two scattering mechanisms and the dominant role of periodic scattering mechanism in this superimposing morphology. However, different from the case $\lambda = 600$ nm, the discrete peaks of ADF_6 reduce to three, because the number of m satisfying Eq. (6) declines to three. Besides, the angle range, which the random features influences, shrinks to around 46°, the major part of the random scattering light stays in the angle range below the first discrete peak (θ=27.8°), and the overlapping region in which both two mechanisms affects is limited to 15°. This result suggests that when light is partly scattered, the random features and periodic features can contribute independently to the total light-trapping, which can explain why $H_6(\lambda)$ almost equals the sum of $H_4(\lambda)$ and $H_5(\lambda)$ in the long wavelength region.

3.3. Different kinds of superimposing morphologies

In this section, we further consider the superimposing morphologies comprised of the same periodic nanostructures in Subsection 3.2 and the other three types of random morphologies: type B, type C, and type D, of which the root-mean-square roughness values vary from a level much lower than the height of the hemisphere (59 nm) to a level very close to the height of the hemisphere (195 nm). To uncover the changes of the scattering properties, we calculate the integrals of the ADFs of all the interfaces from the TCO layer into the silicon absorber under two conditions: (a) $\lambda = 600$ nm, at which light is totally scattered by the superimposing morphologies; (b) $\lambda = 800$ nm, at which light is partly scattered by the superimposing morphologies. The results are shown in Fig. 8.

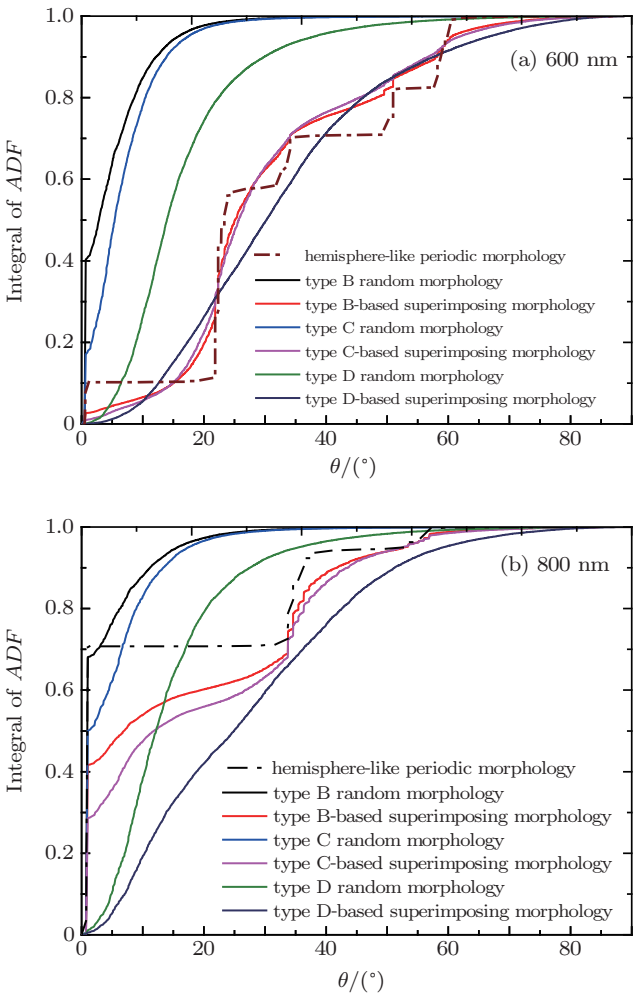


Fig. 8. (color online) Integrals of the ADFs in Fig. 6: (a) $\lambda = 600$ nm and (b) $\lambda = 800$ nm.

At $\lambda = 600$ nm, as the random morphology changes from type B to type D, the total amount of the scattering light increases from 60% to 100%, which already exceeds the amount in the periodic structure, and the angle range extends from 30° to 55°, which also overlaps with the angle range in the periodic structure. This result suggests that the scattering capacity of the random morphology has caught up with that of the periodic morphology or even surpassed it as the random morphology changes to type D. In the integral profiles of the superimposing morphologies corresponding to type B and type C, a slight sharp rise at the discrete angle $\theta = 22.7°$ can still be seen but it disappears completely in the integral profiles of the superimposing morphologies corresponding to type D, which demonstrates that the random scattering mechanism starts to play a dominant role. At $\lambda = 800$ nm, a similar transition of the leading role between the two mechanisms exists. Comparing the integral curves of the periodic structure with those of the superimposing morphologies, it can be found that the periodic structure contribution at θ=32.8° is largely transformed into the angle range from 32.8° to 54.1° in the cases of type B and type C, and it turns negligible in the case of type D. No matter which scattering mechanism dominates, the integrals of *ADF*s of these three types of superimposing morphologies shift into larger angles at different degrees, and this indicates that the combination of the random nanostructure with the periodic nanostructure leads to the further enhancement of the light-trapping in solar cells.

4. Conclusion

In this article, a new kind of morphology is proposed, in which both random nanostructures and period nanostructures are superimposed. Its scattering properties are studied and compared with those of the individual random and period structures, showing that the superimposing structure possesses both scattering mechanisms, and it can scatter the light in the low angle region into a higher angle region by means of the diffraction scattering mechanism and scatter the light around the diffraction peaks into a wide distribution by means of the random scattering mechanism. So this new structure can help to achieve better light trapping in thin film silicon solar cells. Four different random morphologies are also combined with the period morphologies to form superimposing morphologies, and the results show that the scattering properties of the superimposing morphology will approach the individual one whose geometrical features play a leading role, and this rule can help to design other new morphologies.

References

[1] Sai H, Jia H and Kondo M 2010 *J. Appl. Phys.* **108** 044505
[2] Lin C C, Liu W L and Hsieh C Y 2011 *J. Appl. Phys.* **109** 014508
[3] Steinhauser J, Fay S, Oliveira N, Vallat-Sauvain E and Ballif C 2006 *Appl. Phys. Lett.* **90** 142107
[4] Chun B S, Wu H C, Abid M, Chu I C, Serrano-Guisan S, Shvets I V and Choi D S 2010 *Appl. Phys. Lett.* **97** 082109
[5] Berginski M, Hupkes J, Gordijn A, Reetz W, Watjen T, Rech B and Wuttig M 2008 *Sol. Energy Mater. Sol. Cells* **92** 1037
[6] Battaglia C, Hsu C M, Soderstrom K, Escarre J, Haug F J, Charriere M, Boccard M, Despeisse M, Alexander D T L, Cantoni M, Cui Y and Ballif C 2012 *Nano. Lett.* **6** 2790
[7] Sai H, Fujiwara H, Kondo M and Kanamori Y 2008 *Appl. Phys. Lett.* **93** 143501
[8] Zhu J, Hsu C M, Yu Z, Fan S and Cui Y 2010 *Nano Lett.* **10** 1979
[9] Yu Z and Fan S 2011 *Appl. Phys. Lett.* **98** 011106
[10] Battaglia C, Boccard M, Haug F J and Ballif C 2012 *J. Appl. Phys.* **112** 094504
[11] Isabella O, Krc Janez and Zeman M 2010 *Appl. Phys. Lett.* **97** 101106
[12] Battaglia C, Escarre J, Soderstrom K, Charriere M, Despeisse M, Haug F J and Ballif C 2011 *Nat. Photon.* **5** 535
[13] Battkau K, Schulte M, Klein M, Beckers T, Carius R 2011 *Thin Solid Films* **519** 6538
[14] Battaglia C, Soderstrom K, Escarre J, Haug F J, Domine D, Cuony P, Boccard M, Bugnon G, Denizot C, Despeisse M, Feltrin A and Ballif C 2010 *Appl. Phys. Lett.* **96** 213504
[15] Domine D, Haug F J, Battaglia C and Ballif C 2010 *J. Appl. Phys.* **107** 044504
[16] Harvey J E, Vernold C L, Krywonos A and Thomposon P L 1999 *Appl. Opt.* **38** 6469
[17] Krc J, Zeman M, Smole F and Topic M 2002 *J. Appl. Phys.* **92** 749
[18] Bittkau K, Bottler W, Ermes M, Smirnov V and Finger F 2012 *J. Appl. Phys.* **111** 083101
[19] Ding K, Kirchartz T, Pieters B E, Ulbrich C, Ermes A M, Schicho S, Lambertz A, Carius R and Rau U 2011 *Sol. Energy Mater. Sol. Cells* **95** 3318
[20] Soderstrom K, Haug F J, Escarre J, Cubero O and and Ballif C 2010 *Appl. Phys. Lett.* **96** 213508